PCCP

Accepted Manuscript

ROYAL SOCIETY OF CHEMISTRY

www.rsc.org/pccp

Physical Chemistry Chemical Physics

Cite this: DOI: 10.1039/c0xx00000x

www.rsc.org/pccp

PAPER

Experimental and theoretical study of enol-keto prototropic tautomerism and photophysics of azomethine-BODIPY dyads†

Zhong-Hua Pan,[a] Jing-Wei Zhou[b] and Geng-Geng Luo,*[a]

Received (in XXX, XXX) Xth XXXXXXXXX 2014, Accepted Xth XXXXXXXXX 2014
First published on the web Xth XXXXXXXXX 2014
DOI: 10.1039/b000000x

In this study we report about two novel azomethine-BODIPY dyads **1** and **2**. The two dyads have been respectively synthesized by covalent tethering of tautomeric *ortho*-hydroxy aromatic azomethine moieties including *N*-salicylideneaniline (**SA**) and *N*-naphthlideneaniline (**NA**) to a BODIPY fluorophore. Both of the two dyads **1** and **2** show *enol-imine* (OH) structures dominating in the crystalline state. Dyad **1** in the *enol* state is the most stable form at room temperature in most medium, while *enol-keto* prototropic tautomerism of **NA** moiety in solution is preserved in the dyad **2**, which can be reversibly converted between *enol* and *keto* forms in the environment's polarity. Visible illumination of the dyad **2** in the *enol* state excites selectively the BODIPY fragment and then deactivates radiatively by emitting green light in the form of fluorescence, while the emission intensity of **2** in the *keto* state is quenched on the basis of proton-coupled photoinduced electron transfer (PCPET) mechanism. This allows large fluorescence modulation between the two states of the dyad **2** and generates a novel tautomerismable fluorescent switch. Theroretical calculations including calculated energies, potential energy surface (PES) and intrinsic reaction coordinate (IRC) analysis further support single proton transfer reaction from *enol* form to transition state (TS) and from the TS to *keto* form for **2** is easier to occur than that of **1**, which accounts for the fluorescence quenching of **2** in methanol. The agreement of the experimental results and theoretic calculations clearly suggests that fluorescent and tautomeric components can be paired within the same molecular skeleton and the proton tautomerization of the latter can be designed to regulate the emission of the former. In addition, preliminary experiments revealed that **1** can be potentially used as a simple on/off fluorescent chemosensor which exhibited higher selectivity for Cu^{2+} over other common cations.

1. Introduction

Tautomers are readily interconverted constitutional isomers, usually distinguished by a rearrangement of a labile hydrogen atom and a double bond (e.g., *enol-keto* tautomerization).[1] The equilibrium between tautomers is often rapid under normal conditions, being catalyzed by traces of acid or base present in most samples and solvents.[2] Proton tautomerization is central to several fields of chemistry and biochemistry and plays a role in pharmaceutical action, enzyme activity, stabilization of base pairs in duplex DNA, and self-assembly.[3,4] *Ortho*-hydroxy aromatic azomethines (known as Schiff bases) possessing intramolecular hydrogen-bonding are an interesting class of compounds for theoretical and experimental studies because they can undergo proton-tautomerism reaction leading to interesting properties including thermo- and phtochromism. As proton transfer in these systems causes a change in optical properties, these molecules can be utilized for the design of various optical switches and storage devices.[5] According to significances of proton transfer and tautomerism processes, there have been the subject of numerous studies of the *ortho*-hydroxy aromatic azomethines in the solid-state and in solution. Generally, they display two possible tautomeric forms, the *enol-imine* (OH) form and the *keto-enamine* (NH) form. Depending on the tautomers, two types of intramolecular hydrogen bonds are observed in the *ortho*-hydroxy aromatic Schiff bases: O-H···N in *enol-imine* and N-H···O in *keto-enamine* tautomers. The *enol-imine* form is the most stable form at room temperature but is in equilibrium with the *keto-enamine* form relying on the substitution patterns of the aromatic rings and the surrounding medium.[6] Different analytical methods have been used to show the presence of the *enol-imine* and *keto-enamine* forms, among them are UV-vis, fluorescence, Raman, FT-IR, NMR spectroscopy and X-ray crystallography techniques, as well as combinations thereof.[7] As a complement to these experiments, a variety of computational chemistry methods also has been applied.[8] Both experimental and theoretical investigations have shown that the reversible *enol-keto* tautomerism occurs via an intramolecular H-transfer mechanism between the *ortho*-hydroxy and the imine nitrogen.[8] *Enol-keto*

[a] *College of Materials Science and Engineering, Huaqiao University, Xiamen 361021, P. R. China*; *E-mail: ggluo@hqu.edu.cn; Fax: 86-592-6162225.*
[b] *School of Pharmaceutical Sciences, East Campus, Sun Yat-sen University, Guangzhou 510006, P. R. China*

† Electronic Supplementary Information (ESI) available. Additional calculations and experimental measurements, figures and tables. CCDC reference numbers 1000809-1000810. For ESI and crystallographic data in CIF or other electronic format see DOI:10.1039/b000000x.

tautomerism has been used to modulate magnetic dynamics of some lanthanide complexes.[9] However, relatively less attention has been paid to attachment of *ortho*-hydroxy azomethine fragments into organic chromophores to study the effect of *enol*↔*keto* tautomerism reaction on photophysical properties of chromophores.

Seeking to look for suitable organic chromorphores in favor of grafting tautomeric components, our attention has turned to the boron dipyrromethene (4,4-difluoro-4-bora-3*a*,4*a*-diaza-*s*-indacene, BDP or BODIPY) class of dyes. Recent efforts in other groups and our laboratory have focused on developing BODIPY fluorescence sensors based on photoinduced electron transfer (PET) as a transduction mechanism.[10] BODIPYs are well-known for their excellent photophysics such as strong absorption of visible light, high fluorescence quantum yields and good photostability.[10,11] In addition, the optical properties of BODIPY are tunable through structural modifications on the core of dye. These favorable features render BODIPY as widely used as a fluorophore core for the construction of luminophores, molecular probes or molecular logic gates, light-harvesting molecular arrays and photodynamic therapy (PDT) agents.[11] In this context, we decided to explore the possibility of integrating fluorescent and tautomeric components within the same molecular skeleton. We report herein the synthesis, structures, photophysical properties of two dyads (**1** and **2**) with high thermal stabilities, which consist of *ortho*-hydroxy aromatic azomethines including *N*-salicylideneaniline (**SA**) and *N*-naphthlideneaniline (**NA**) coupled to a BODIPY fluorophore. Significant differences in the photophysical behaviours of the synthesized two dyads related with proton-tautomerism are observed and discussed with the aid of density functional theory (DFT) calculations.

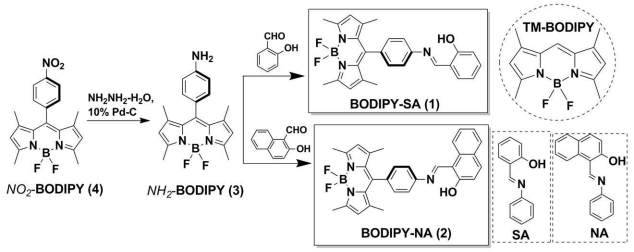

Scheme 1 Design and synthesis of dyads **1** and **2**.

2. Result and discussion

2.1. Synthesis and characterization

The starting BODIPY-linked aniline **3** was firstly synthesized in moderate yield from a reaction of 2,4-dimethylpyrrole and 4-nitro-benzaldehyde, followed by a conversion of the $-NO_2$ group to form an $-NH_2$ substitute according to reported procedures.[10e,12] With the main aim of investigating the effect of prototropic tautomerism of *ortho*-hydroxy aromatic Schiff bases on the photophysics of BODIPY chromophores, azomethine-BODIPY dyads **1** and **2** functionalized with imines were prepared by convenient one-step condensation reaction of **3** with 2-hydroxybenzaldehyde or 2-hydroxynaphthaldehyde in a high yield according to the synthetic procedures along with individual Schiff bases (**SA** and **NA**) as well as a model **TM-BODIPY**, as shown in Scheme 1. Dyads **1** and **2** were first documented from single-crystal X-ray crystallography (SCXRD) and further characterized by standard analytical techniques (i.e., FT-IR spectra, NMR spectroscopy, mass spectrometry, elemental analysis and cyclic voltammetry), which gave satisfactory data corresponding to their molecular structures. Solid-state IR spectra of **1** and **2** were recorded in the 4000-400 cm^{-1} region (Fig. S1 of ESI†). Generally, the non-hydrogen-bonded or a free hydroxyl group absorbs strongly in the 3550-3700 cm^{-1} region.[13] Intramolecular hydrogen bonding if present in the six-membered ring system would reduce the O-H stretching band to 3550-3200 cm^{-1} region.[14] IR spectra of **1** and **2** show a sharp band at 3441 and 3442 cm^{-1} due to O-H stretching vibration. The characteristic region of 1700-1500 cm^{-1} can be used to identify the proton transfer of Schiff bases. Azomethine (C=N) bond stretching vibration was observed to be 1623 and 1626 cm^{-1} for **1** and **2**. The crystal phase purities of **1** and **2** were confirmed from powder X-ray diffraction (PXRD) patterns (Fig. S2 of ESI†). The thermal behavior of **1** and **2** as well as **SA** and **NA** was studied by differential scanning calorimetry (DSC) (Fig. S3 of ESI†). The DSC thermogram of **1** and **2** exhibited only one exothermic peak at 288 ºC (ΔH = 107.9 J g^{-1}) and 299 ºC (ΔH = 86.21 J g^{-1}), respectively, ascribed to the melting point (T_m) of dyads. Obviously, the two dyads exhibit the higher melting point and more stable than that of starting material **3** (T_m = 190 ºC) or references of Schiff bases **SA** (T_m = 52±1 ºC) and **NA** (T_m = 96±1 ºC).

The redox behaviour of the two dyads were investigated using the cyclic voltammetry (CV) technique in dry DCM containing 0.1 M TBAP background electrolyte (Table S1 of ESI†). For these dyads, a single electrochemically peak is observed on reductive scans that could be ascribed to formation of the BODIPY π-radical anion (-1.69 V for **1** and -1.59 V for **2**). On oxidative scans, two peaks corresponding to the oxidation of Schiff base fragment, and the formation of the BODIPY π-radical cation are observed for **1** and **2**. For **2**, slight negative shift of oxidation peak from Schiff base fragment (0.62 V) compared with that of **1** (0.80 V) due to the redundant benzene ring. The oxidation potentials of BODIPY moiety in these dyads is similar (1.01 V for **1**, and 1.04 V for **2**). From these results of electrochemistry, it is inferred that the Sciff base unit and BODIPY group are isolated and only minor, if any, electronic communication takes place through the bridge in the groud state.

2.2. Crystal structural analyses

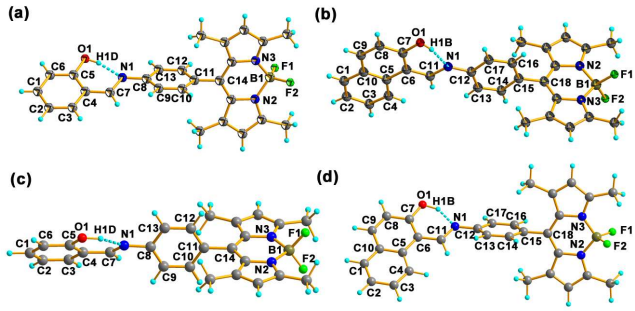

Fig 1 Single crystal X-ray diffraction structures of **1** (a), **2** (b) with thermal ellipsoids set at 50% probability, and the theoretical geometric structures of **1** (c) and **2** (d).

Crystalline samples of azomethine-BODIPY dyads **1** and **2** were obtained by a slow vapour diffusion of hexane into a saturated $CHCl_3$ solution of **1** or CH_2Cl_2 solution of **2**. Single crystals collected were of suitable quality to undertake a structure determination by SCXRD analysis, and crystallographic data are given in Table S2 (ESI†). Both **1** and **2** crystallize in the triclinic space group $P\bar{1}$ with one independent molecule within the asymmetric unit (Fig. 1a, b). In fact, each azomethine-BODIPY dyad constitutes a BODIPY unit as the fluorophore and a Schiff base fragment as tautomerism. As previously observed in some similar structures,[10d,15] the BODIPY core $B(N_2F_2)$ shows a quasi-tetrahedron configuration with the average angle of F-B-F of 108.8º and the average bond length of B-N and B-F to be 1.544 Å and 1.388 Å, respectively (Table S3 of ESI†). On the BODIPY moiety, the C_9BN_2 framework consisting of one central six-membered and two adjacent five-membered rings is essentially flat, with the maximum deviation from the least-squares mean plane for the 12 atoms of the indacene group being 0.083 Å in **1** and 0.029 Å in **2**, respectively. This geometry indicates the strongly delocalized π-system nature of the C_9BN_2 framework in **1** and **2**. However, this π-electron delocalization is interrupted between the two B-N bonds (1.536-1.554 Å), which is in agreement with the results reported for other BODIPYs.[15] Introduction of two methyl groups at C-1 and C-7 positions in the BODIPY core in **1** and **2** were revealed to prevent the free rotation of the *meso*-phenyl moiety, resulting in almost orthogonal configuration between the BODIPY core and *meso*-benzene moiety. The dihedral angle between the *meso*-phenyl ring and the indacene plane (87.6º) in **1**, is analogous to that in **2** (86.5º), indicating the almost nonelectronic coupling nature between the *meso*-phenyl ring and C_9BN_2 unit in **1** and **2**.

From the ORTEP view, the dihedral angle between the aromatic ring systems in the Schiff base moiety of **1** is 26.1º. This dihedral angle decreases to 4.1º in **2**. In general, *ortho*-hydroxy Schiff bases undergo tautomerism involving proton transfer from the hydroxylic oxygen to the imino nitrogen atom. The process of proton transfer ends up with two tautomeric forms known as *enol* and *keto* structure. The C7-N1 and C5-O1 bond for **1** as well as C11-N1 and C7-O1 bond for **2** are the most important indicators of the tautomeric types. The C5-O1 and C7-O1 bond are of double bonds for the *keto-enamine* tautomers, whereas these bonds display single bond character in the *enol-imine* tautomers. The C7-N1 and C11-N1 bond are also double bonds in the *enol-imine* tautomers and of single bond length in the *keto-enamine* tautomers. SCXRD reveals the preference of *enol* structure in the Schiff base moiety in the solid state for **1** and **2**, as indicated by the bond parameters (C5-O1 = 1.359 Å, C7-O1 = 1.329 Å and C7-N1 = 1.285 Å, C11-N1 = 1.291 Å). Furthermore, the aromaticities of *enol* forms of **1** and **2** can be also inferred from the harmonic oscillator model aromaticity (HOMA) index.[16] The HOMA indices in the range of 0.900-0.990 and 0.500-0.800 correspond to aromatic and the non-aromatic rings, respectively. In **1**, the calculated HOMA indices for C1/C6 and C8/C13 are 0.968 and 0.992. These results show that C1/C6 and C8/C13 in **1** have purely aromatic character. In **2**, the calculated HOMA indices for C5/C10 and C12/C17 are 0.629 and 0.995, which display that C12/C17 has purely aromatic character while C5/C10 is deviated from aromaticity. This difference in molecular configuration is responsible for different results of theoretical calculations and optical properties as discussed below.

Table 1 Experimental and theoretical hydrogen-bond geometries (Å, deg) for **1** and **2**.

D-H···A	D-H	H···A	D···A	D-H···A
X-ray diffraction for **1**	1.02(4)	1.65(5)	2.605(4)	153.8(3)
B3LYP/6-31+G(d,p) for **1**	1.00	1.74	2.634	147.2
X-ray diffraction for **2**	1.02(2)	1.61(3)	2.548(2)	150.9(2)
B3LYP/6-31+G(d,p) for **2**	1.01	1.65	2.563	148.0

The existence of strong intramolecular O1-H1D···N1 and O1-H1B···N1 hydrogen bonds both producing *S*(6) ring motifs is observed in **1** and **2**, respectively. These H-bonds can be characterized by O1···N1 distances and are summarized in Table 1. It is known that there is a strong correlation between the strength of the H-bond and the delocalization of the system of conjugated double bonds, and the effect is qualitatively interpreted by resonance-assisted hydrogen bond (RHAB) model.[17] The observed O···N distance of 2.605(4) Å for **1** and 2.548(2) Å for **2** are apparently shorter than 2.656 Å which was reported for O-H···N in the class of RAHB model. The aggregations of **1** and **2** through a series of weak hydrogen bonds including C-H···F and edge-face C-H···π interactions in the crystal cells are shown in Fig. S4 of ESI†. These F- and C-based interactions can be further visualized by Hirshfeld surface calculations and given in Fig. S5 of ESI†.

2.3. Computational studies

The optimized parameters (bond lengths, bond angles, and dihedral angles) of dyads **1** and **2** have been obtained using the *Gaussian 09* program with density functional theory (DFT), the B3LYP method, and 6-31+G(d,p) as the basis set. The optimized structures of **1** and **2** are depicted in Fig. 1c and Fig. 1d with numbering of the atoms. The calculated structural parameters of **1** and **2** are presented in Table S3 along with the corresponding values obtained from the experimental data. When the X-ray structures of **1** and **2** are compared to their optimized counterparts, the bond lengths and bond angles

computed by B3LYP method show a good correlation with the experimental values. The remarkable conformational discrepancies are observed in the orientation of *meso*-phenyl ring in **1** and **2**. The orientation of *meso*-phenyl ring is defined by the torsion angles C7-N1-C8-C13 [153.1(2)º for **1**] and C11-N1-C12-C17 [177.2(1)º for **2**]. These torsion angles have been calculated at 145.06º and 146.11º for B3LYP, respectively. Such conformational discrepancies can be explained by the fact that the calculations assume an isolated molecule where the intermolecular Coulombic interaction with the neighboring molecules are absent, whereas the experimental result corresponds to interacting molecules in the crystal lattice, as described in the aforementioned crystal structure analysis. When the geometries of hydrogen bond in the optimized structures of **1** and **2** are examined, it is seen that O-H···N intramolecular hydrogen bonds exist between the phenol O atom for **1** (naphthol O atom for **2**) and imine N atom. For **1**, O-H, H···N, and O-H···N values are 1.02(4) Å, 1.65(5) Å, and 153.8(3)º for X-ray diffraction, and 1.00 Å, 1.74 Å, and 147.2º for B3LYP. For **2**, O-H, H···N, and O-H···N values are 1.02(2) Å, 1.61(3) Å, and 150.9(2)º for experimental data, and 1.01 Å, 1.65 Å, and 148.0º for theoretical values. There are good matching between the calculated hydrogen-bond geometries and those obtained from the X-ray diffraction structures. The presence of the hydrogen bond appears as an important property of the molecule, stabilizing its conformation in the crystal; as shown in the molecular modelling part, this is also visible in the model obtained for the molecules discussed.

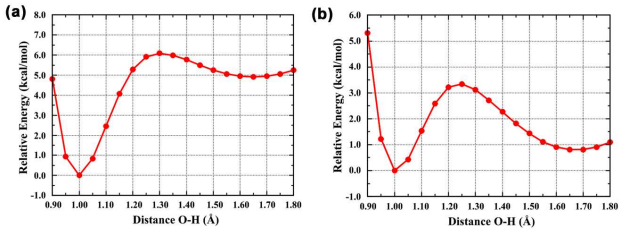

Fig 2 Relative energy profiles during the proton transfer process of **1** (a) and **2**(b).

The *enol-imine* (NH) and *keto-enamine* (OH) tautomerisms of dyads **1** and **2** are given in Scheme S1. To investigate these tautomeric stabilities, quantum chemical calculations were carried out for the *enol* and *keto* forms of **1** and **2**. Some important physicochemical properties such as total, HOMO, and LUMO energies and dipole moment (μ) were also calculated with the same level of theory, and the results are given in Table 2. First comparing the total energies of the two tautomers for **1**, the *enol* tautomer is substantially more stable (4.91 kcal mol^{-1}) than the *keto* form. This is an expected result since the *enol* form of **1** has two purely aromatic rings as supported by the above structural analysis and *ortho*-hydroxy azomethine generally prefers the *enol* structure. The intramolecular proton transfer for **1** was investigated in the gas phase by performing a potential energy surface (PES) scan process at the B3LYP/6-31+G(d,p) level in order to determine its effects on the molecular geometry. The process was started from optimized *enol-imine* geometry by selecting O-H bond as redundant internal coordinate. The graph of the relative energy versus the O-H bond distances is given in Fig. 2. The energy values were calculated relative to the energy of the stable *enol* form. Fig. 2a shows two minima representing the stable forms of **1**. The *keto* form corresponds to a local minimum while the global minimum represents the stable *enol* form. The potential energy barrier needed for the *enol* to *keto* form conversion process in **1** was calculated as 6.08 kcal mol^{-1}.

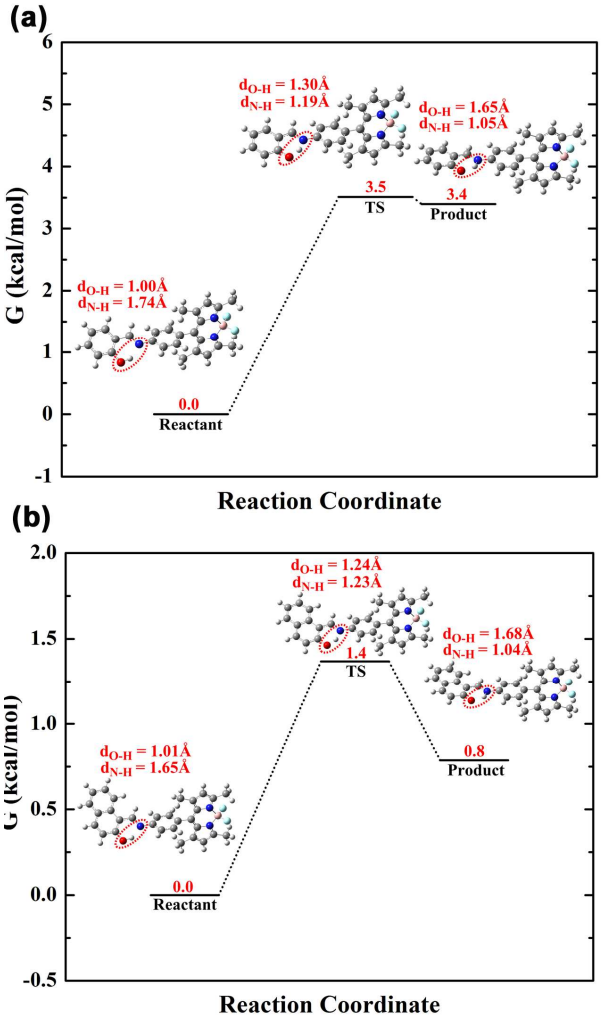

Fig 3 Transition state from enol to keto form of **1** (a) and **2**(b) at the B3LYP/6-31+G(d,p) level (kcal mol^{-1}).

We have also considered **2** for further study to know whether the nature of proton transfer of **1** and **2** is the same. As seen from Table 2, the calculated total energy of the *enol* form of **2** is only slightly lower than the *keto* form in the gas phase (0.81 kcal mol^{-1}). Similar to the dyad **1**, PES scan of **2** shows two distinct minima corresponding to *enol* and *keto* tautomers. Here the *enol* form is slightly stable than *keto* form. The energy barrier in going from *enol* to *keto* form is 3.34 kcal mol^{-1}, which is obviously smaller than that of **1**. Such a small energy barrier is easily overcome by a light-weight particle, such as a proton at room temperature. Therefore, at ground state there will be always a mixture of *keto* and *enol* forms with larger percentage

of *enol* form in gas phase and *keto* form in solution, respectively.

To further examine the whole process of *enol-keto* tautomerization via single proton transfer in the dyads **1** and **2** in more detail, we performed an intrinsic reaction coordinate (IRC) analysis for each case (see Supporting Information). The nature of the stationary points was confirmed by means of a vibrational analysis. The whole prototropic tautomerism process of **1** and **2** is actually subdivided into two parts: (i) transfer from the *enol* form (OH) to the transition state (TS), and (ii) from the TS to the proton transfer *keto* form (NH). Fig. 3 shows calculated free energy profiles and the structures of *enol* form, TS, and *keto* form for **1** and **2**. For *enol-keto* tautomerization of **1**, the free energy of *keto* form is very close to that of TS (3.4 kcal mol^{-1} *vs* 3.5 kcal mol^{-1}) while large than which of *enol* form (3.4 kcal mol^{-1} *vs* 0 kcal mol^{-1}). While for **2**, both the barrier energy and product free energy are on the verge of the reactant free energy (1.4 kcal mol^{-1} *vs* 0.8 kcal mol^{-1} *vs* 0 kcal mol^{-1}). These calculated results indicate that compared to **1**, the single proton transfer reaction of **2** is easier to occur, and **2** is more inclined to obtain an *enol-keto* mixture while **1** not. A closer analysis of structures, we can see both the structures of reactants and transition states of **1** and **2** exist different while the product states are similar. For reactant state, the distance of N-H hydrogen-bond of reaction center in **1** is larger than that in **2**, indicating that the proton transfers from O atom to N atom is more relaxed in **2**. For TS, the distance of N-H and O-H are equivalent in **2** while in **1** the distance of O-H is larger than that of N-H, indicating that the structure of TS is similar to the structure of product state in **1** and to some extent means that the proton-tranfer-distance from reactant to TS in **1** is longer than that in **2**. Therefore, the single proton transfer reaction of **2** is easier to occur. The reason of this result may owe to the redundant benzene ring of **2** which could increase the conjugative effect and resonant structure compared to **1** (Fig. S6 of ESI†).

Table 2 Calculated energies, dipole moments, and frontier orbital energies in vacuum and in methanol for **1-2** and their tautomers.

	Tautomer	E_{TOTAL} (hartree)	E_{HOMO} (eV)	E_{LUMO} (eV)	μ (D)
Gas phase (ε =1)	**1**-*enol*	-1469.54123405	-5.6793	-2.7007	4.8157
	1-*keto*	-1469.53340411	-5.7579	-2.7884	3.8781
	2-*enol*	-1623.18996163	-5.6602	-2.6814	5.4163
	2-*keto*	-1623.18870347	-5.7209	-2.7483	4.4635
CH_3OH (ε = 32.7)	**1**-*enol*	-1469.55686104	-5.8172	-2.8177	6.7180
	1-*keto*	-1469.55389163	-5.8317	-2.8398	5.5145
	2-*enol*	-1623.20631485	-5.8143	-2.8145	7.2598
	2-*keto*	-1623.20871348	-5.8153	-2.8313	5.9880

2.4. Photophysical properties

The optical properties of **1** and **2** were first characterized by using UV-vis absorption in solvents of varying polarity (Table 3 and Fig. S7 of ESI†). Fig. 4 shows the absorption spectra of **1** and **2** as well as references **SA** and **NA** in CH_3OH. The absorption spectra of the studied dyads exhibit features that can be easily assigned to specific subunits. **SA** exhibits two moderate absorption peaks centered at 269 nm and 348 nm, respectively, assignable to $\pi\rightarrow\pi^*$ and $n\rightarrow\pi^*$ transition.[18] The model **TM-BODIPY** presents a sharp and intense absorption peak at 500 nm (Fig. S8 of ESI†),[19] a typical feature for the BODIPY dyes.[15] The absorption spectrum of the dyad **1** is nearly the superposition of the spectra of **SA** and **TM-BODIPY**. The absorption maximum (499 nm) of **1** with molar absorptoin coefficient as high as 8.03×10^4 M^{-1} cm^{-1} is as expected for **TM-BODIPY** dye, which is due to the 0-0 vibrational band of the $S_0\rightarrow S_1$ (π-π^*) transition localized on the BODIPY unit.[19]

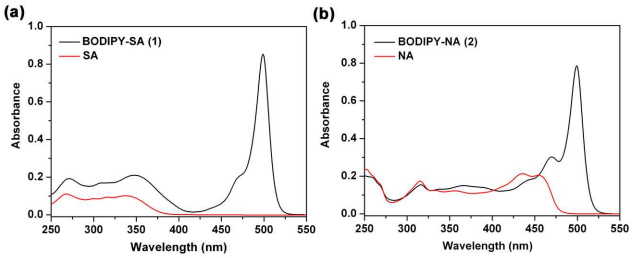

Fig 4 UV-Vis absorption spectra of **1** and **SA** (a) as well as **2** and **NA** (b) in methanol at room temperature, path length 1.0 cm, concentration 1×10^{-5} M for each sample.

Table 3 Spectral parameters of **1** and **2** in different solvents.

	Solvent	$E_T(30)^a$ (kcal mol^{-1})	λ_{abs} (max/nm)	Log (ε_{max})	λ_{em} (max/nm)	$\Phi_{fl}{}^b$
1	MeOH	55.4	499	4.92	512	0.38
	CH_3CN	45.6	498	4.93	511	0.48
	THF	37.4	501	4.95	515	0.53
	CH_2Cl_2	40.7	502	4.95	516	0.55
	toluene	33.9	505	4.92	518	0.57
2	MeOH	55.4	499	4.93	513	0.05
	CH_3CN	45.6	498	4.94	512	0.03
	THF	37.4	501	4.95	516	0.30
	CH_2Cl_2	40.7	502	4.95	516	0.27
	toluene	33.9	505	4.96	519	0.40

[a]Solvent polarity index. [b]1,3,5,7-tetramethyl-8-phenyl-BODIPY was used as a standard (Φ_{fl} = 0.72 in tetrahydrofuran).

Dyad **2** also shows an intense absorption band centered at 499 nm with absorption coefficient around 7.97×10^4 M^{-1} cm^{-1}. In addition, **2** displays a shoulder at the short wavelength (high-energy) side, is centered at about 469 nm, and is attributed to the 0-1 vibrational band of the same transition. The moderate higher-energy transitions of **NA** unit in **2** were observed at 315 and 375 nm, attributed to π-π^* transition of *enol* form of **NA**. Interestingly, an absorption band at 438 nm was observed in the spectrum of **2** in CH_3OH, which may belong to the *keto* form of *ortho*-hydroxy Schiff bases.[20] In contrast, any band belonging to *keto-enamine* form in **1** was not observed with a value greater than 400 nm. Referring to previous studies it was concluded that **2** exists in both *enol* and *keto* form in CH_3OH while **1** is in favor of the *enol* state and not in *keto* in most organic solvents at room temperature.[8a,21] The *keto* form is important in the solution and stabilized by the polar solvents through solute-solvent interactions. Here hydrogen bonding between hydroxyl group of methanol and nitrogen atom of Schiff base has played

a crucial role in the proton transfer process. It can be noted that in these dyads there is not any significant absorption band which can not be assigned to specific individual subunits: this suggests that the interaction among the various components is weak and attachment of the Schiff base fragment to the BODIPY entity causes minimal perturbation of its optical properties, so that these dyads can be regarded as multicomponent systems.

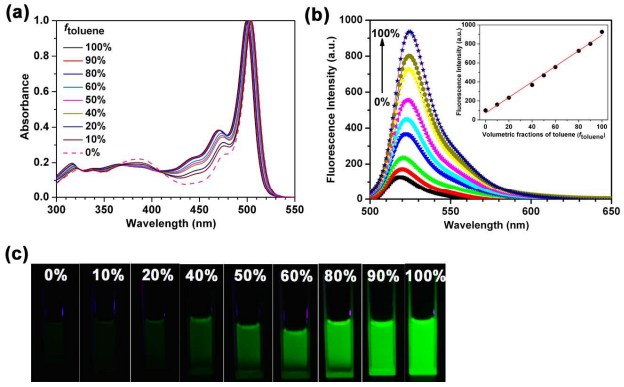

Fig 5 (a) Absorption spectra and (b) fluorescence spectra (λ_{ex} = 470 nm) of **2** in toluene-methanol mixtures with volume ratios of toluene; (c) photographs of the solutions of **2** in a mixture of methanol-toluene solvent system with different toluene fraction taken under UV illumination.

For a better understanding of the experimental data on the optical properties, the optimizations of both *keto* and *enol* forms of **1** and **2** were carried out with the B3LYP/6-31+G(d,p) level using polarizable continuum model (PCM) in the presence of methanol (ε = 32.7) (Table 2). Our theoretical results allow the conclusion that the total energy of the *enol* form of **1** obtained by PCM method is still more stable than the *keto* form, though both HOMO and LUMO energy values become more and more negative in going from gaseous phase to solution phase with the increase of dielectric constant value. However, calculated energies of **2** in methanol show that the *enol-imine* form is less stable than the *keto-enamine* form by 6.30 kJ mol^{-1}, which indicate that it is energetically favorable to have carbon-carbon double bonds rather than carbon-nitrogen double bonds. In other words, the process of intramolecular proton transfer evoked by the influence of solvent results in destabilization of the OH form (a decrease in the prevalence of the OH form and an increase in that of the NH form) and destabilization of aromatic formation. Thus, *keto-enamine* form of **2** is much more stable than *enol-imine*, which accounts for available UV-Vis experimental results.

Steady-state fluorescence spectra of **1** and **2** were also measured in various solvents with increasing polarity from toluene to methanol, and the details data are gathered in Table 2 and Fig. S9 (ESI†). From the viewpoint of fluorescence, the structures of BODIPY-linked Schiff bases can be composed of two fragments, the BODIPY moiety as a fluorophore and Schiff base moiety as a fluorescence switch, which modulates the fluorescence quantum yield (Φ_{fl}) of the fluorophore, since they are orthogonal to each other. The starting material **3** was reported to display quenched emission in methanol with Φ_{fl} < 1%.[10e] The quenching phenomenon has all the hallmarks of photoinduced electron transfer (PET) from the phenylamino unit to the boradizaindacene fluorophore. Upon condensation with salicydehyde to form **1**, the reduction potential of the non-bonding electron pair on nitrogen atom decreased due to the formation of an imine functional group. In other words, electron transfer from the electron-deficient imine moiety to the electron-rich BODIPY fluorophore became less feasible. Frontier orbital diagram also indicates that the highest occupied molecular orbital (HOMO) energy of phenylamino unit (-5.38 eV) was higher than the HOMO energy of imine (-6.26 eV), thereby preventing PET quenching of the emission, exhibiting the photoluminescence quantum efficiencies vary between 0.57 and 0.38 (Table 3).

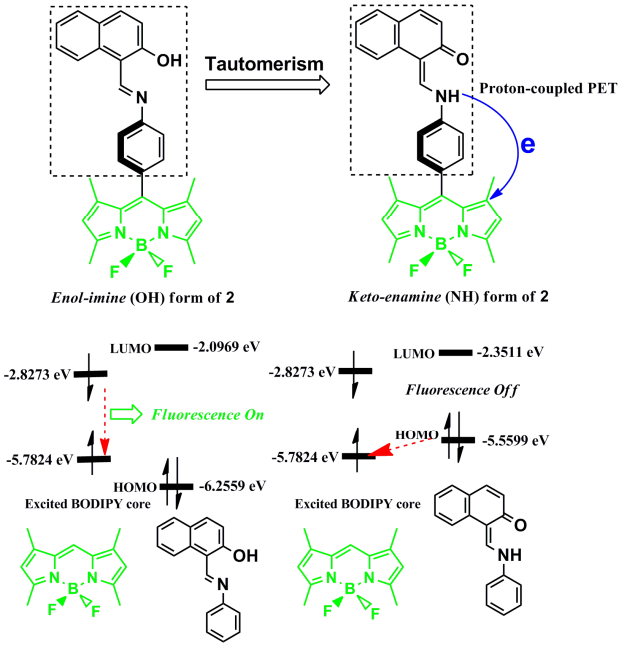

Fig 6 Proposed proton-coupled photoinduced electron transfer (PCPET) mechanism between BODIPY moiety and *keto* unit of **2**.

In contrast, for **2**, the value of Φ_{fl} is up to 0.40 in toluene, and declines to only 0.05 in methanol. We speculate that the marked difference in fluorescence quantum yields between **1** and **2** in pure methanol is consistent in the prototropic tautomerism, and derives from an increase in *keto* form for **2** compared with that of its analog **1**. In order to experimentally strengthen the above speculation, the photo-physical properties of **2** had been studied in a mixture of methanol-toluene, in which the toluene content ($f_{toluene}$) was varied in the range of 0-100 vol%. The UV-Vis spectra of **2** in the methanol-toluene solvent system showed several isosbestic points at 410, 364, and 324 nm, which definitely point out the existence of two molecular absorbing species in equilibrium (Fig. 5a). The luminescent properties of **2** were also investigated in the methanol-toluene system and the results are given in Fig. 5b. The emission intensity of **2** increased dramatically as the fraction of toluene $f_{toluene}$ increased, and the logarithm of the intensity and the fraction have a good linear relationship with $R^2 > 0.99$ as shown in

the inset of Fig 5b. The visual emission color of **2** in the methanol-toluene system when excited at a hand-held 365 nm UV lamp is shown in Fig 5c, which is consistent with the above analysis. Overall, these findings of fluorescence contrast with the above observations of UV-Vis spectra. Therefore, **1** retains a moderate fluorescence quantum yield while the lower value of Φ_{fl} for **2** indicates a highly efficient fluorescence quenching by a thermodynamically allowed proton-coupled photoinduced electron transfer (PCPET) from the *keto* unit of **NA** to the singlet excited state of the BODIPY moiety.

To shed light on the photoinduced activation of an electron transfer process within an azomethine-BODIPY dyad, computations on the **1** and **2** before and after prototropic tautomerism are also performed and displayed in Fig. S10 (ESI†) and Fig. 6. As shown in Fig. 6, before prototropic tautomerism of **2**, the HOMO energy level of *enol* form of **NA** moiety (-6.26 eV) is obviously lower than that of the BODIPY unit (-5.78 eV); therefore, the PET process can be suppressed and the emission of BODIPY fluorophore is on. The energy level of HOMO (-5.56 eV) of *keto* form of **NA** moiety should increase above that of the HOMO (-5.78 eV) of the fluorophore BODIPY only after prototropic tautomerism. Under these conditions, the electron transfer process becomes exoergonic and favorable. As a consequence, when the BODIPY moiety of **2** is photoexcited, one electron can be transferred from the *keto* form of **NA** to the BODIPY moiety with a concomitant fluorescence quenching.

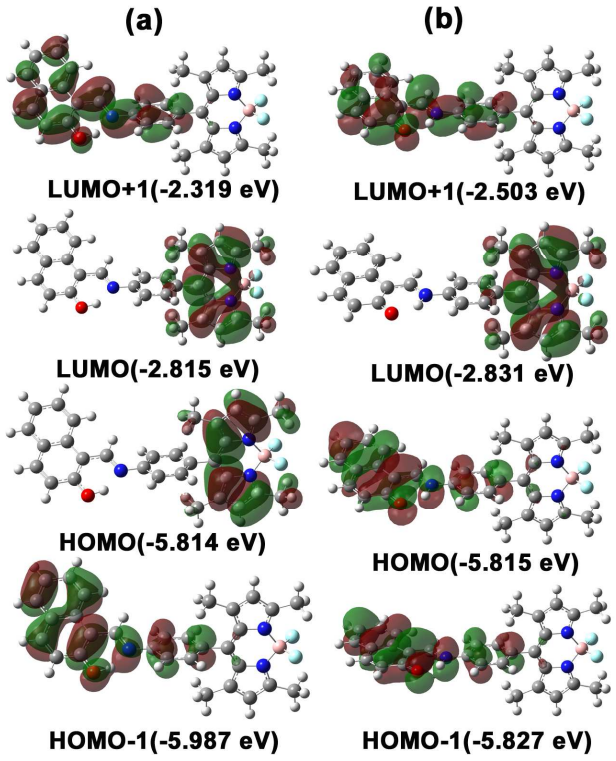

Fig 7 Molecular orbital surfaces and energy levels given in parentheses for LUMO+1, LUMO, HOMO, and HOMO-1 of *enol* and *keto* form of **2** computed at the B3LYP/6-31+G(d,p) in methanol solvent.

The calculated frontier molecular orbital (FMO) energies and surfaces of **2** are shown in Fig. 7. As can be found, both the contours of the electronic distribution in HOMO and LUMO states of **2** in the *enol* form are located almost completely on the BODIPY moiety, while the HOMO-1 and LUMO+1 are located mainly on the **NA** fragment. It is postulated that the HOMO-LUMO transition corresponds to the emissive $\pi\rightarrow\pi^*$ excited state as observed in the reference dye **TM-BODIPY** and other BODIPY derivatives.[10] As a result, the electronic transition between HOMO and LUMO for **2** in the *enol* form is limited only on the BODIPY moiety, leading to an intensive intrinsic fluorescence from the BODIPY moiety of **2** in the *enol* form. By contrast, the calculation results reveal that both the LUMO and HOMO-1 orbitals for **2** in the *keto* form are mostly contributed from the BODIPY moiety, while the HOMO and LUMO+1 orbitals are mainly located at the **NA** fragment. The significant distribution difference between HOMO and LUMO of **2** in the *keto* form shows that there is electron transfer from the **NA** fragment (*keto* form) to the BODIPY core. And this is likely related to the PET process between the **NA** fragment (*keto* form) and BODIPY core, which quenches the fluorescence of BODIPY component.

2.5. Dyad 1 as 'on-off' fluorescent chemosensor for Cu^{2+}

Dyad **1** was preliminarily chosen to detect metal ions based on the following considerations: (1) as described in the foregoing discussion, **1** in the *enol-imine* state is the most stable form at room temperature in solution and shows moderate fluorescence quantum yields in most medium compared to dyad **2**. (2) Schiff bases are well known to be good ligands for metal ions, and Schiff bases incorporating a fluorescent moiety are appealing tools for optical sensing of metal ions.[22]

Initially, the absorption and fluorescence response of **1** toward the nitrate salts of Cu^{2+}, Ag^{+}, Al^{3+}, Ca^{2+}, Co^{2+}, Cr^{3+}, Fe^{3+}, Li^{+}, Mg^{2+}, Mn^{2+}, Na^{+}, Ni^{2+}, Pb^{2+}, and Zn^{2+} were carried out in a MeOH/$CHCl_3$ (20:1, v/v) solution (Fig. 8a and Fig. S11). Changes of the fluorescence properties of **1** caused by various metal ions were measured once emission intensity was constant. When 1 equiv. of Cu^{2+} was added to the solution of **1**, the fluorescent intensity will be reduced by 80%, which suggested that **1** showed a particular response to Cu^{2+} ions compared to those of other metal ions of similar electronic structure. It is well-known that the paramagnetic Cu^{2+} center has a pronounced quenching effect on fluorophores through a photoinduced electron or energy transfer mechanism.[23] Additionally, among the relevant paramagnetic metal ions, Cu^{2+} has a particularly high thermodynamic affinity for ligands with N or O as chelating element, and fast metal-to-ligand binding kinetics process.[24]

Selectivity is a matter of necessity for a chemosensor. To investigate the selectivity of **1** for Cu^{2+} over other relevant cations, the fluorescent intensity changes upon addition of various competitive cations were examined, 3 equiv. of most other metal ions showed no interference to the sensing of Cu^{2+} by **1**. Additionally, to explore the effects of anionic counterions on the sensing behavior of **1** to metal ions, fluorescence

responses of **1** to chloride, nitrate, perchlorate and sulfate salts with Cu^{2+} were examined and it can be seen that anions had no influence on the fluorescence of **1** (Fig. S12). The fluorescence intensity of **1** exhibits gradual reduction upon the addition of 0-1.0 equiv of Cu^{2+} and saturation upon the addition of 1.0-3.0 equiv of Cu^{2+}, revealing that the stoichiometry of the complex formed between **1** and Cu^{2+} ions is 1:1 (Fig. 8b). Overall, current preliminary experiments revealed that **1** can be potentially used as a simple fluorescent chemosensor which exhibited high selectivity for Cu^{2+} over other common cations. To further confirm the quenching mechanism, the coordination environment of the **1**/Cu^{2+} complex and the corresponding association constant (*K*), more experiments including Job's method, ESI-MS, X-ray crystallography and NMR titration as well as DFT calculations are currently in progress.

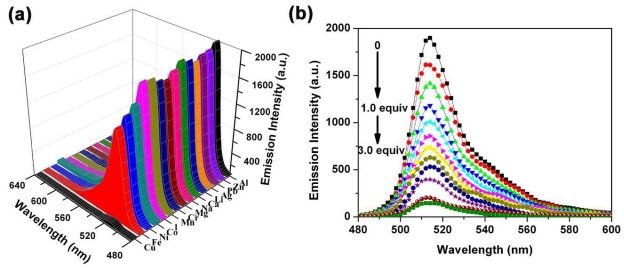

Fig 8 (a) Emission spectra of **1** (1.0×10^{-5} M) in the solution of MeOH/$CHCl_3$ (20:1, v/v) upon addition of 3 equiv of different metal nitrate salts; (b) fluorescent spectra of **1** (1.0×10^{-5} M, excited at 470 nm) upon addition of 0-1.0 equiv of Cu^{2+}.

3. Conclusions

Two new dyads made of azomethine and BODIPY subunits, **1**-**2**, have been prepared, together with their parent species **SA**, **NA** and **TM-BODIPY**, and the photophysical properties of all the compounds have been investigated in fluid solution. Weak electronic interactions between Schiff base units and BODIPY fragments take place in the ground states of the two dyads, whose absorption spectra resemble those of their constituting groups. The marked difference in luminescence between **1** and **2** in methanol is observed and obviously consistent in the prototropic tautomerism of **2**. Irradiation of the dyad **2** in the *enol* state excites the BODIPY component, which then returns to its ground state by emitting light in the form of fluorescence. However, the *keto* state of **2** can donor an electron to the excited fluorophore. As a result of the proton-coupled photoinduced electron transfer (PCPET) process, the excited state of the BODIPY component is quenched and the associated fluorescence suppressed. Theoretical calculations of total energies, potential energy surface (PES) and intrinsic reaction coordinate (IRC) analysis also support single proton transfer reaction from *enol* form to transition state (TS) and from the TS to *keto* form for **2** is easier to occur than that of **1**, which accounts for the fluorescence quenching phenomenon of **2**. Additionally, **1** was preliminarily chosen as on/off type of fluorescent chemosensor for Cu^{2+} over other common cations.

This contribution not only attempts to integrate fluorescent and tautomeric components within the same molecular skeleton, but also presents the proton tautomerization can be designed to regulate the emission of an organic chromophore between a nonemissive state and an emissive one. In addition, in view of *ortho*-hydroxy aromatic Schiff bases exhibiting the interesting phenomena of photochromism,[25] the detailed investigation of the relationship between fluorescence modulation and photochromic behavior of these azomethine-BODIPY dyads as well as other BODIPY-linked Schiff bases both in solution and in the solid state when exposed to light of different wavelengths is under progress in our laboratory.

4. Experimental

4.1. Materials

All the materials for the syntheses were purchased from commercial suppliers and used without further purification. Air- and moisture-sensitive reactions were carried out under a nitrogen atmosphere using oven-dried glassware. Solvents were dried by standard literature methods[26] before being distilled and stored under nitrogen over 3Å molecular sieves prior to use. Water was deionized. Thin-layer chromatography (TLC) was performed using silica gel plates and flash column chromatography was conducted over silica gel (200-300 meshes) with the eluent reported in parentheses, both of which were obtained from the Qingdao Ocean Chemicals.

4.2. Instrumentation

^1H and ^{13}C NMR spectra were recorded at room temperature using a Bruker PLUS 400 spectrometer with tetramethylsilane (TMS, 0.00 ppm) as an internal standard and $CDCl_3$ as solvent. Chemical shift multiplicities are reported as s = singlet, d = doublet, and br = broad singlet. Coupling constants (*J*) values are given in Hz. Mass spectrometry (MS) experiment was carried out in the positive ion made on a Bruker Esquire HCT ion trap mass spectrometer (Billerica, MA) coupled with a homemade electrospray ionization (ESI) device. Parameters of the ESI source were optimized to enhance the signal intensity. The pressure of nebulizing nitrogen, the flow rate of desolvation gas, and the temperature of desolvation gas were set to 8 psi, 1L min^{-1}, and 250 ºC, respectively. Electrochemical experiments were performed using a three-electrode system. The working electrode was 2 mm Pt with a Pt wire as auxiliary electrode and a 0.01M $Ag/AgNO_3$ solution reference electrode. The sample solution contained an azomethine-BODIPY (1.0×10^{-3} M) and 0.1 M tetrabutylammonium hexafluorophosphate (TBAP) as a supporting electrolyte in dry acetonitrile. FT-IR spectra were recorded from KBr pellet in the range 4000-400 cm^{-1} on a Nicolet AVATAT FT-IR360 spectrometer. C, H, and N microanalyses were carried out with a CE instruments EA 1110 analyzer. The experimental powder X-ray diffraction patterns were measured on a Panalytical X-Pert Pro diffractometer with Cu Kα radiation equipped with an X'Celerator detector. Differential scanning calorimetry (DSC) data were measured on a Netzsch-DSC-200F3 instrument at the heating rate of 10 ºC min^{-1} from 25 to 310 ºC. Samples were heated in open aluminum pans under a nitrogen gas flow of 20 mL min^{-1}.

4.3. Spectroscopic measurements and determination of fluorescent quantum yields

Azomethine-BODIPYs were dissolved in various solvents to acquire optical measurements. Acetonitrile, methanol, tetrahydrofuran, dichloromethane and toluene were all individually used in preparing a BODIPY solution. UV-vis absorption and steady-state fluorescence spectroscopic studies are performed on a UV-2100 (Shimadzu) spectrophotometer and a F-7000 (Hitachi) spectrophotometer at room temperature. The slit width was 5 nm for both excitation and emission. Samples for absorption and emission measurements were contained in 1 cm × 1 cm quartz cuvettes. Measurements were made using optically dilute solutions after deoxygenation by purging with dried N_2.

The relative fluorescence quantum yields (Φ_{fl}^{sample}) of the samples were obtained by comparing the area under the corrected emission spectrum of the test sample with that of a standard. Only dilute solutions with an absorbance below 0.1 at the excitation wavelength λ_{ex} were used. The Φ_{fl}^{sample} values were calculated using synthesized 8-phenyl-4,4-difluoro-1,3,5,7-tetramethyl 4-bora-3a,4a-diaza-*s*-indacene (compound **3**, $\Phi_{fl}^{standard}$ = 0.72 in tetrahydrofuran)[27] as fluorescence standard using the following equation:

$$\Phi_{fl}^{sample} = \Phi_{fl}^{standard} \times (I^{sample}/I^{standard}) \times (A^{standard}/A^{sample}) \times (n^{sample}/n^{standard})^2$$

Where Φ_{fl}^{sample} and $\Phi_{fl}^{standard}$ are the emission quantum yields of the sample and the reference, respectively, $A^{standard}$ and A^{sample} are the measured absorbances of the reference and sample at the excitation wavelength, respectively, $I^{standard}$ and I^{sample} are the area under the emission spectra of the reference and sample, respectively, and $n^{standard}$ and n^{sample} are the refractive indices of the solvents of the reference and sample, respectively. The Φ_{fl}^{sample} values reported in this work are the averages of multiple (generally three), fully independent measurements.

4.4. Synthetic procedures

The syntheses of the starting BODIPY compounds NH_2-BODIPY (**3**) and NO_2-BODIPY (**4**) were achieved using literature methods and characterized by ^{1}H NMR, ^{13}C NMR and elemental analysis to determine their structures.[10e,12]

8-(4-nitro-phenyl)-4,4-difluoro-1,3,5,7-tetramethyl 4-bora-3a,4a-diaza-*s*-indacene (4):. ^{1}H NMR (400 MHz, $CDCl_3$) δ 1.37 (s, 6H), 2.57 (s, 6H), 6.03 (s, 2H), 7.54 (d, 2H, *J* = 8.8 Hz), 8.39 (d, 2H, *J* = 8.8 Hz); ^{13}C NMR (100 MHz, $CDCl_3$) δ 14.5, 121.7, 124.4, 129.6, 130.6, 138.3, 141.9, 142.5, 148.4, 156.3. Anal. Cacld for $C_{19}H_{18}BF_2O_2N_3$: C, 61.81; H, 4.91; N, 11.38. Found: C, 61.78; H, 4.87; N, 11.35.

8-(4-amino-phenyl)-4,4-difluoro-1,3,5,7-tetramethyl 4-bora-3a,4a-diaza-*s*-indacene (3):. ^{1}H NMR (400 MHz, $CDCl_3$) δ 1.51 (s, 6H), 2.57 (s, 6H), 4.44 (br, 2H), 5.99 (s, 2H), 6.86 (d, 2H, *J* = 4.0 Hz), 7.05 (d, 2H, *J* = 6.8 Hz); ^{13}C NMR (150 MHz, $CDCl_3$) δ 14.5, 14.6, 115.5, 119.7, 120.9, 124.7, 128.8, 128.9, 132.0, 142.6, 143.2, 146.9, 154.9. Anal. Cacld for $C_{19}H_{20}BF_2N_3$: C, 67.28; H, 5.94; N, 12.39. Found: C, 67.33; H, 5.91; N, 12.31.

Synthesis of 8-(1-azastyryl(2-hydroxynaphthaldehyde))-4,4-difluoro-1,3,5,7-tetramethyl 4-bora-3a,4a-diaza-*s*-indacene (2): **3** (339 mg, 1 mmol) and 2-hydroxy-1-naphthaldehyde (172 mg, 1 mmol) were refluxed for 6 h under nitrogen atmosphere at 78 ºC in 50 mL of absolute ethanol. When TLC analysis showed that the reaction was complete, the solution was cooled to room temperature. The product was collected by filtration as a red solid. Recrystallization from CH_2Cl_2/EtOH (356 mg, 75% yield); M.p. = 299 ºC. ν_{max}(KBr pellet) cm^{-1}: 3442 (ν_{OH}), 1626 ($\nu_{C=N}$), 1600, 1576, 1548, 1511, 1466, 1408, 1359, 1309, 1257, 1201, 1155, 1117, 1091, 1073, 1038, 983, 893, 829, 803, 767, 744, 707, 506, 477. ^{1}H NMR (400MHz, $CDCl_3$): 1.50 (s, 6H), 2.60 (s, 6H), 6.03 (s, 2H), 7.26 (d, *J* = 9.2 Hz, 1H), 7.41 (t, *J* = 7.7 Hz, 3H), 7.58 (dd, *J* = 17.0, 7.9 Hz, 3H), 7.78 (d, J = 7.9 Hz, 1H), 7.89 (d, *J* = 9.2 Hz, 1H), 8.19 (d, *J* = 8.4 Hz, 1H), 9.48 (s, 1H).

. ^{13}C NMR (100 MHz, $CDCl_3$): δ 14.62, 14.70, 74.34, 76.68, 77.00, 77.21, 77.32, 112.28, 116.48, 121.56, 121.87,126.17, 127.82, 128.49, 129.17, 129.46, 130.92, 132.96, 135.60, 140.29, 148.04, 156.01. ESI-MS *m/z* ($C_{30}H_{26}BF_2N_3O$) calculated: 493.4, found: 516.3 (M+Na), 532.3 (M+K).

Synthesis of 8-(1-azastyryl(2-hydroxybenzaldehyde))-4,4-difluoro-1,3,5,7-tetramethyl 4-bora-3a,4a-diaza-*s*-indacene (1). **3** (339 mg, 1 mmol) and 2-hydroxy-1-benzaldehyde (125 mg, 1 mmol) were refluxed for 6 h under nitrogen atmosphere at 78 ºC in 50 mL of absolute ethanol. When TLC analysis showed that the reaction was complete, the solution was cooled to room temperature. The product was collected by filtration as an orange solid. Recrystallization from $CHCl_3$/EtOH (300 mg, 80% yield); M.p. = 288 ºC. ν_{max}(KBr pellet) cm^{-1}: 3441 (ν_{OH}), 1623 ($\nu_{C=N}$), 1597, 1573, 1545, 1508, 1467, 1409, 1365, 1306, 1279, 1195, 1154, 1120, 1086, 1052, 978, 910, 842, 810, 761, 708, 665, 581, 479. ^{1}H NMR (400MHz, $CDCl_3$): δ 1.48 (s, 6H), 2.59 (s, 6H), 6.03 (s, 2H), 7.00 (t, *J* = 7.5 Hz, 1H), 7.10 (d, *J* = 8.2 Hz, 1H), 7.39 (d, *J* = 8.3 Hz, 2H), 7.41-7.49 (m, 4H), 8.74 (s, 1H), 13.08 (s, 1H). ^{13}C NMR (100 MHz, $CDCl_3$): δ 14.75, 14.64, 76.71, 77.02, 77.23, 77.34, 117.40, 119.03, 119.29, 121.35, 122.00, 129.09, 129.32, 131.46, 132.51, 133.58, 133.66, 140.95, 143.00, 149.10, 155.71, 161.26, 163.45. ESI-MS *m/z* ($C_{26}H_{24}BF_2N_3O$) calculated: 443.3, found: 466.3 (M+Na), 482.3 (M+K).

8-phenyl-4,4-difluoro-1,3,5,7-tetramethyl 4-bora-3a,4a-diaza-*s*-indacene (5) was synthesized according to the literature reports.[15] ^{1}H NMR (400 MHz, $CDCl_3$) δ 1.39 (s, 6H, CH3), 2.58 (s, 6H, CH3), 6.00 (s, 2H), 7.28-7.32 (m, 2H, phenyl), 7.49-7.50 (m, 3H, phenyl); ^{13}C NMR (100 MHz, $CDCl_3$) δ 14.3, 14.6, 121.2, 127.9, 128.9, 129.1, 131.4, 135.0, 141.7, 143.1, 155.4. Anal. Cacld for $C_{19}H_{19}BF_2N_2$: C, 70.40; H, 5.91; N, 8.64. Found: C, 70.44; H, 5.88; N, 8.67. Since **5** is one internal reference dye for the determination of quantum yields and it is regularly checked for stability and purity.

4,4-difluoro-1,3,5,7-tetramethyl 4-bora-3a,4a-diaza-*s*-indacene (the model **TM-BODIPY**) was prepared using a literature procedure.[19] ^{13}C NMR (125 MHz, $CDCl_3$) δ 11.3, 14.6, 119.1, 120.2, 133.3, 141.2, 156.7. ESI-MS *m/z* ($C_{13}H_{15}BF_2N_2$) calculated: 248.1, found: 271.1 (M+Na).

References *N*-salicylideneaniline (**SA**) and *N*-naphthlideneaniline (**NA**) are synthesized by the appropriate condensation of the corresponding aldehyde and aniline according to the standard procedures as previously reported.[8c,28] Pure **SA** and **NA** obtained after recrystallization twice from absolute ethanol. The melting points agreed with those in the

literature and the elemental analyses were in accord. Other analysis data are as follows. **SA**: M.p. 51-53ºC. ^{1}H NMR(400MHz, $CDCl_3$): δ 6.98 (q, 1H, J = 7.3 Hz), 7.09(d, 1H, J = 8.3 Hz), 7.33 (m, 3H), 7.45 (m, 4H), 8.67 (s, 1H). FT-IR transmission (KBr pellet): 3433 cm^{-1} (ν_{OH}), 1615 cm^{-1} ($\nu_{C=N}$), 1590, 1572, 1507, 1496, 1485, 1453, 1402, 1361, 1277, 1186, 1169, 1150, 1116, 1074, 1032, 982, 917, 896, 843, 780, 757, 691, 547, 523 cm^{-1}. UV-Vis, λ_{max}/nm, (ε/L mol^{-1} cm^{-1}), (CH_3OH): 269 nm (11000), 348 nm (10570). Anal. Cacld for $C_{13}H_{11}NO$ (197.23): C, 79.17; H, 5.62; N, 7.10. Found: C, 79.12; H, 5.57; N, 7.02. **NA**: M.p. 95-97ºC. ^{1}H NMR(400MHz, $CDCl_3$): δ 7.14 (d, 1H, J = 9.12Hz), 7.37(d, 2H, J = 8.52Hz), 7.44 (m, 2H, J = 13.48Hz), 7.71 (d, 1H, J = 7.93Hz), 7.80 (d, 1H, J = 9.11Hz), 8.07(d, 1H, J = 8.59Hz). FT-IR transmission (KBr pellet): 3437 cm^{-1} (ν_{OH}), 1626 cm^{-1} ($\nu_{C=N}$), 1570, 1542, 1489, 1476, 1420, 1329, 1248, 1181, 1163, 1076, 1023, 967, 911, 873, 824, 750, 694 cm^{-1}. UV-Vis, λ_{max}/nm, (ε/L mol^{-1} cm^{-1}), (CH_3OH): 315 nm (17283), 357 (12228), 435 nm(22000) and 455 nm(20400). Anal. Cacld for $C_{17}H_{13}NO$ (247.3): C, 82.57; H, 5.30; N, 5.66. Found: C, 82.61; H, 5.35; N, 5.55.

4.5. Crystallization experiments and X-ray crystallography

The quality of single crystals depends on the purity of the used material. Hence, the synthesized target dyads were highly purified (recrystallization at least twice before performing crystallization experiments). Better quality crystals of **1** and **2** were obtained by slow vapour diffusion of n-hexane into a saturated $CHCl_3$ solution of **1** or CH_2Cl_2 solution of **2** at room temperature.

Intensity data for **1** and **2** were collected on a Rigaku R-AXIS RAPID Image Plate single-crystal diffractometer using graphite-monochromated Mo Kα radiation source (λ = 0.71073 Å). Single crystals of **1** and **2** with appropriate dimensions were chosen under an optical microscope and mounted on a glass fiber for data collection at low temperature (173 ± 2K). Absorption correction was applied by correction of symmetry-equivalent reflections using the ABSCOR program.[29] All structures were solved by direct methods using SHELXS-97[30] and refined by full-matrix least-squares on F^2 using SHELXL-97[31] via the program interface X-Seed.[32] Non-hydrogen atoms were refined anisotropically. Hydrogen atoms attached to oxygen in **1** and **2** were located by difference Fourier maps and other hydrogen atoms were isotropically in a riding model with U_{iso} values 1.2-1.5 times those of their parent atoms. All structures were examined using the Addsym subroutine PLATON[33] to ensure that no additional symmetry could be applied to the models. Crystal structure views were obtained using Diamond v3.1.[34] Details of the data collection conditions and the parameters of the refinement process are given in Table S2. Selected bond lengths and angles are listed in Table S3. The hydrogen bond geometries for **1** and **2** are shown in Table 1.

4.6. Computational details

Theoretical calculations have been performed with the *Gaussian 09* software package.[35] For the purpose of accordance with experimental results, the molecular structures of **1** and **2** are taken from the crystal structures before optimization. The geometry optimization of enol and keto forms as well as the transition states (TS) of **1** and **2** in gas phase is performed by carrying out density functional theory (DFT) calculations with Becke's three-parameter exchange and Lee-Yang-Parr correlation functionals (B3LYP) with a combination of 6-31+G(d,p) basis set. The harmonic vibrational frequencies of the studied structures are calculated at the same level to characterize their existence on the potential energy surface (PES). The minimum energy structures are ensured by the absence of any imaginary frequency whereas any transition state is characterized by the presence of only one imaginary frequency. In solution phase, the geometry optimization of the studied structures is performed at the same level with polarizable continuum model (PCM). All molecular orbitals were visualized with the software *GaussView* 5.0.

Acknowledgements

This work was financially supported by the National Natural Science Foundation of China (no. 21201066), the Natural Science Foundation of Fujian Province (no. 2011J01047), the outstanding Youth Scientific Research Cultivation Plan of Colleges and Universities of Fujian Province (JA13008), and Promotion Program for Young and Middle-aged Teacher in Science and Technology Research of Huaqiao University (ZQN-PY104). Dr. Hai-Feng Su (Xiamen University) is greatly acknowledged for assistance with the ESI-MS experiments and we thank Dr. Hong-Xin Mei (Xiamen University) for help with the single-crystal X-ray diffraction data collections. Zhong-Hua Pan also thanks the National Innovative Foundation Project for undergraduates (no. 201310385004).

Notes and references

(1) J. Toullec, *Adv. Phys. Org. Chem*., 1982, **18**, 1-261.
(2) (a) S. K. Pollack and W. J. Hehre, *J. Am. Chem. Soc*., 1977, **99**, 4845-4846; (b) H. E. Zimmermann, *Acc. Chem. Res*., 1987, **20**, 263-268; (c) J. Toullec and J. E. Dubois, *J. Am. Chem. Soc*., 1974, **96**, 3524-3532.
(3) (a) R. Glaser and M. Lewis, *Org. Lett*., 1999, **1**, 273-276; (b) R. S. Phillips, B. Sundararaju and N. G. Faleev, *J. Am. Chem. Soc*., 2000, **122**, 1008-1014; (c) P. T. Chou, Y. C. Chen, C. Y. Wei and W. S. Chen, *J. Am. Chem. Soc*., 2000, **122**, 9322-9323; (d) O. K. Abou-Zied, R. Jimenez and F. E. Romesberg, *J. Am. Chem. Soc*., 2001, **123**, 4613-4614; (e) P. Naumov, A. Sekine, H. Uekusa, Y. Ohashi, *J. Am. Chem. Soc*., 2002, **124**, 8540-8541; (f) M. J. Thompson, D. Bashford, L. Noodleman and E. D. Getzoff, *J. Am. Chem. Soc*., 2003, **125**, 8186-8194.
(4) (a) D. S. Lawrence, T. Jiang and M. Levett, *Chem. Rev*., 1995, **95**, 2229-2260; (b) R. P. Sijbesma and E. W. Meijer, *Curr. Opin. Colloid Interface Sci*., 1999, **4**, 24-32; (c) L. Forlani, E. Mezzina, C. Boga and M. Forconi, *Eur. J. Org. Chem*., 2001, 2779-2785; (d) G. M. Whitesides and B. Grzybowski, *Science*, 2002, **295**, 2418-2421.
(5) (a) B. L. Feringa, W. F. Jager and B. de Lange, *Tetrahedron* 1993, **49**, 8267-8470; (b) K. Nakatani and J. A. Delaire, *Chem. Mater*., 1997, **9**, 2682-2684; (c) J. Harada, H. Uekusa and Y. Ohashi, *J. Am. Chem. Soc*., 1999, **121**, 5809-5810; (d) H. Pizzala, M. Carles, W. E. E. Stone and A. Thevand, *J. Chem. Soc., Perkin Trans. 2*, 2000, 935-939; (e) K. Ogawa, J. Harada, T. Fujiwara and S. Yoshida, *J. Phys. Chem. A*, 2001, **105**, 3425-3427; (f) V. Vargas and L. Amigo, *J. Chem. Soc., Perkin Trans. 2*, 2001, **2**, 1124-1134; (g) K. Amimoto, H. Kanatomi, A. Nagakari, H. Fukuda, H. Koyama and T. Kawato, *Chem. Commun*., 2003, 870-871; (h) J. H. Chong, M. Sauer, B. O. Patrick and M. J. MacLachlan, *Org. Lett*., 2003, **5**, 3823-3826.

(6) (a) T. Suzuki and T. Arai, *Chem. Lett*., 2001, 124-127; (b) J. J. Charette and E. De Hoffmann, *J. Org. Chem*., 1979, **44**, 2256-2262; (c) P. E. Hansen, F. Duus and P. Schmitt, *Org. Magn. Reson.,* 1982, **18**, 58-61.

(7) (a) H. Ünver, *Spectrosc. Lett*., 2001, **34**, 783-791; (b) S. R. Salman, J. C. Lindon and R. D. Farrant, *Magn. Reson. Chem.,* 1993, **31**, 991-994; (c) S. H. Alarcon, A. C. Olivieri and A. Nordon, *Tetrahedron* 1995, **51**, 4619-4626; (d) J. W. Ledbetter, *J. Phys. Chem*., 1982, **86**, 2449-2451; (f) V. Vargas C., *J. Phys. Chem. A*, 2004, **108**, 281-288; (e) M. Sliwa, S. Létard, I. Malfant, M. Nierlich, P. G. Lacroix, T. Asahi, H. Masuhara, P. Yu and K. Nakatani, *Chem. Mater*., 2005, **17**, 4727-4735; (f) H. Tanak, *J. Phys. Chem. A*, 2011, **115**, 13865-13876.

(8) (a) L. Antonov, W. M. F. Fabian, D. Nedeltcheva and F. S. Kamounah, *J. Chem. Soc., Perkin Trans. 2*, 2001, **2**, 1173-1179; (b) S. H. Alarcón, A. C. Olivieri and M. González-Sierra, *J. Chem. Soc., Perkin Trans. 2*, 1994, **2**, 1067-1070; (c) W. M. F. Fabian, L. Antonov, D. Nedeltcheva, F. S. Kamounah and P. J. Taylor, *J. Phys. Chem. A*, 2004, **108**, 7603-7612; (d) A. Filarowski and I. Majerz, *J. Phys. Chem. A*, 2008, **112**, 3119-3126; (e) P. I. Nagy and W. M. F. Fabian, *J. Phys. Chem. B*, 2006, **110**, 25026-25032.

(9) Y. N. Guo, X. H. Chen, S. F. Xue and J. K. Tang, *Inorg. Chem*., 2011, **50**, 9705-9713.

(10) (a) G. Ulrich, R. Ziessel and A. Harriman, *Angew. Chem. Int. Ed.*, 2008, **47**, 1184-1201; (b) N. Boens, V. Leen and W. Dehaen, *Chem. Soc. Rev*., 2012, **41**, 1130-1172; (c) T. Ueno, Y. Urano, H. Kojima and T. Nagano, *J. Am. Chem. Soc*., 2006, **128**, 10640-10641; (d) G. G. Luo, J. X. Xia, K. Fang, Q. H. Zhao, J. H. Wu and J. C. Dai, *Dalton Trans*., 2013, **42**, 16268-16271; (e) Z. H. Pan, G. G. Luo, J. W. Zhou, J. X. Xia, K. Fang and R. B. Wu, *Dalton Trans*., 2014, **43**, 8499-8507; (f) H. Lu, S. S. Zhang, H. Z. Liu, Y. W. Wang, Z. Shen, C. G. Liu and X. Z. You, *J. Phys. Chem. A*, 2009, **113**, 14081-14086.

(11) (a) A. Loudet and K. Burgess, *Chem. Rev*., 2007, **107**, 4891-4932; (b) A. Kamkaew, S. H. Lim, H. B. Lee, L. V. Kiew, L. Y. Chung and K. Burgess, *Chem. Soc. Rev*., 2013, **42**, 77-88; (c) A. C. Benniston and G. Copley, *Phys. Chem. Chem. Phys*., 2009, **11**, 4124-4131.

(12) A. Cui, X. Peng, J. Fan, X. Chen, Y. Wu and B. Guo, *J. Photochem. Photobiol*., A, 2007, **186**, 85-92.

(13) A. Teimouri, A. N. Chermahini, K. Taban, H. A. Dabbagh, *Spectrochim. Acta, Part A*, 2009, **72**, 369-377.

(14) H. A. Dabbagh, A. Teimouri, A. N. Chermahini, M. Shahraki, *Spectrochim. Acta, Part A*, 2008, **69**, 449-459.

(15) (a) Z. Chen, H. Rohr, K. Rurack, H. Uno, M. Spieles, B. Schulz and N. Ono, *Chem.-Eur.J.*, 2004, **10**, 4853-4871; (b) M. Broring, R. Kruger, S. Link, C. Kleeberg, S. Kohler, X. Xie, B. Ventura and L. Flamigni, *Chem.-Eur.J*., 2008, **14**, 2976-2983; (c) X. D. Yin, Y. J. Li, Y. L. Zhu, X. Jing, Y. L. Li and D. B. Zhu, *Dalton Trans*., 2010, **39**, 9929-9935.

(16) HOMA index was defined by the formulas: HOMA = $1-\frac{1}{n}\sum_{i=1}^{n}\alpha_i(R_{opt}-R_i)^2$, where n represents the total number of bonds in the ring, R_i is an individual bond length, α_i is an empirical constant equal to 257.7 and R_{opt} is equal to 1.388 Å for CC bonds. For purely aromatic compounds, HOMA index is equal to 1 while it is equal to 0 for nonaromatic compounds. See: (a) T. M. Krygowski, *J. Chem. Inf. Comput. Sci*., 1993, **33**, 70-78; (b) T. M. Krygowski and M. K. Cyrański, *Chem. Rev*., 2001, **101**, 1385-1419.

(17) G. Gilli and P. Gilli, *J. Mol. Struct*., 2000, **552**, 1-15.

(18) J. W. Ledbetter, *J. Phys. Chem*., 1966, **70**, 2245-2249.

(19) L. X. Wu and K. Burgess, *Chem. Commun*., 2008, 4933-4935;

(20) (a) H. Ünver, M. Kabak, M. D. Zengin and T. N. Durlu, *J. Chem. Crystallogr*., 2001, **31**, 203-209; (b) H. Ünver, M. Yildiz, M. D. Zengin, S. Özbey and E. Kendi, *J. Chem. Crystallogr*., 2001, **31**, 211-216.

(21) R. Gawinecki, A. Kuczek, E. Kolehmainen, B. Ośmiałowski, T. M. Krygowski and R. Kauppinen, *J. Org. Chem*., 2007, **72**, 5598-5607.

(22) (a) Y. Dong, J. Li, X. Jiang, F. Song, Y. Cheng and C. Zhu, *Org. Lett*., 2011, **13**, 2252-2255; (b) S. Kim, J. Y. Noh, K. Y. Kim, J. H. Kim, H. K. Kang, S. W. Nam, S. H. Kim, S. Park, C. Kim and J. Kim, *Inorg. Chem*., 2012, **51**, 3597-3602.

(23) (a) Q. Y. Wu, E. V. Anslyn, *J. Am. Chem. Soc*., 2004, **126**, 14682-14683; (b) M. H. Lim, B. A. Baik and S. J. Lippard, *J. Am. Chem. Soc*., 2006, **128**, 14364-14373.

(24) (a) R. Krämer, *Angew. Chem. Int. Ed*., 1998, **37**, 772-773; (b) J. Hu, F. T. Lü, L. P. Ding, S. J. Zhang, Y. Fang, *J. Photochem. Photobiol. A*, 2007, **188**, 351-357.

(25) (a) E. Hadjoudis and I. M. Mavridis, *Chem. Soc. Rev*., 2004, **33**, 579-588; (b) K. M. Hutchins, S. Dutta, B. P. Loren and L. R. MacGillivray, *Chem. Mater*., 2014, doi: 10.1021/cm500823t.

(26) J. A. Riddick, W. B. Bunger, T. K. Sakano, *Organic Solvents*, 4th ed.; Wiley-Interscience, New York, 1986.

(27) Y. C. Wang, D. K. Zhang, H. Zhou, J. L. Ding, Q. Chen, Y. Xiao and S. X. Qian, *J. Appl. Phys*., 2010, **108**, 455-462.

(28) H. E. Smith, S. L. Cook and M. E. Warren, *J. Org. Chem*., 1964, **29**, 2265-2267.

(29) T. Higashi, *ABSCOR*, Empirical Absorption Correction based on Fourier series Approximation; Rigaku Corporation: Tokyo, 1995.

(30) G. M. Sheldrick, *SHELXS-97*, Program for X-ray Crystal Structure Determination; University of Gottingen: Germany, 1997.

(31) G. M. Sheldrick, *SHELXL-97*, Program for X-ray Crystal Structure Refinement; University of Gottingen: Germany, 1997.

(32) L. J. Barbour, X-Seed, A software tool for Supramolecular Crystallography; *Supramol. Chem*. 2001, **1**, 189-191.

(33) A. L. Spek, Implemented as the *PLATON* Procedure, a Multi-purpose Crystallographic Tool; Utrecht University: Utrecht, The Netherlands, 1998.

(34) K. Brandenburg, *DIAMON*D, Version 3.1f; Crystal Impact GbR: Bonn, Germany, 2008.

(35) M. J. Frisch, G. W. Trucks, H. B. Schlegel, G. E. Scuseria, M. A. Robb, J. R. Cheeseman, G. Scalmani, V. Barone, B. Mennucci, G. A. Petersson, H. Nakatsuji, M. Caricato, X. Li, H. P. Hratchian, A. F. Izmaylov, J. Bloino, G. Zheng, J. L. Sonnenberg, M. Hada, M. Ehara, K. Toyota, R. Fukuda, J. Hasegawa, M. Ishida, T. Nakajima, Y. Honda, O. Kitao, H. Nakai, T. Vreven, J. A. Montgomery Jr,., J. E. Peralta, F. Ogaliaro, M. Bearpark, J. J. Heyd, E. Brothers, K. N. Kudin, V. N. Staroverov, R. Kobayashi, J. Normand, K. Raghavachari, A. Rendell, J. C. Burant, S. S. Iyengar, J. Tomasi, M. Cossi, N. Rega, J. M. Millam, M. Klene, J. E. Knox, J. B. Cross, V. Bakken, C. Adamo, J. Jaramillo, R. Gomperts, R. E. Stratmann, O. Yazyev, A. J. Austin, R. Cammi, C. Pomelli, J. W. Ochterski, R. L. Martin, K. Morokuma, V. G. Zakrzewski, G. A. Voth, P. Salvador, J. J. Dannenberg, S. Dapprich, A. D. Daniels, O. Farkas, J. B. Foresman, J. V. Ortiz, J. Cioslowski and D. J. Fox, *Gaussian*, Inc., Wallingford CT., 2009.

Graphical Abstract

Enol↔keto prototropic tautomerism can be exploited to modulate the photophysics of BODIPY chromophores based on proton-coupled photoinduced electron transfer processes.